Preclinical Pharmacokinetics and Biodistribution Studies of [89]Zr-Labeled Pembrolizumab

Christopher G. England*[1], Emily B. Ehlerding*[1], Reinier Hernandez[1], Brian T. Rekoske[2], Stephen A. Graves[1], Haiyan Sun[3], Glenn Liu[2,4], Douglas G. McNeel[2,4], Todd E. Barnhart[1], and Weibo Cai[1,3,4]

[1]Department of Medical Physics, University of Wisconsin–Madison, Madison, Wisconsin; [2]Department of Medicine, University of Wisconsin–Madison, Madison, Wisconsin; [3]Department of Radiology, University of Wisconsin–Madison, Madison, Wisconsin; and [4]University of Wisconsin Carbone Cancer Center, Madison, Wisconsin

Pembrolizumab is a humanized monoclonal antibody targeting programmed cell death protein 1 (PD-1) found on T and pro-B cells. Pembrolizumab prevents PD-1 ligation by both PD-L1 and PD-L2, preventing the immune dysregulation that otherwise occurs when T-cells encounter cells expressing these ligands. Clinically, PD-1 blockade elicits potent antitumor immune responses, and antibodies blocking PD-1 ligation, including pembrolizumab, have recently received Food and Drug Administration approval for the treatment of advanced melanoma, renal cell cancer, and non–small cell lung cancer. **Methods:** In this study, we evaluated the pharmacokinetics, biodistribution, and dosimetry of pembrolizumab in vivo, accomplished through radiolabeling with the positron emitter [89]Zr. PET imaging was used to evaluate the whole-body distribution of [89]Zr-deferoxamine (Df)-pembrolizumab in two rodent models (mice and rats). Data obtained from PET scans and biodistribution studies were extrapolated to humans to estimate the dosimetry of the tracer. As a proof of concept, the biodistribution of [89]Zr-Df-pembrolizumab was further investigated in a humanized murine model. **Results:** The tracer remained stable in blood circulation throughout the study and accumulated the greatest in liver and spleen tissues. Both mice and rats showed similar biodistribution and pharmacokinetics of [89]Zr-Df-pembrolizumab. In the humanized mouse model, T-cell infiltration into the salivary and lacrimal glands could be successfully visualized. **Conclusion:** These data will augment our understanding of the pharmacokinetics and biodistribution of radiolabeled pembrolizumab in vivo, while providing detailed dosimetry data that may lead to better dosing strategies in the future. These findings further demonstrate the utility of noninvasive in vivo PET imaging to dynamically track T-cell checkpoint receptor expression and localization in a humanized mouse model.

Key Words: positron emission tomography (PET); [89]Zr; pembrolizumab; programmed cell death protein 1 (PD-1); dosimetry

Over the last five years, immunotherapies have shown remarkable success for the treatment of many cancers. Cancer immunotherapies encompass a broad range of therapeutic approaches with a similar end goal, namely directing the body's immune system to kill tumor cells (1). However, as cancers derive from patients' own cells, tumor cells maintain many natural autoimmune defense mechanisms that can prevent tumor immune destruction. Disruption of these autoimmune defensive mechanisms has been shown to be remarkably successful at eliciting antitumor responses against many types of cancers (2). Two of these most studied pathways, known as immune checkpoint pathways, are the cytotoxic T-lymphocyte–associated antigen 4 (CTLA-4) and programmed cell death protein 1 (PD-1). Both CTLA-4 and PD-1 are receptors expressed on the surface of activated T-cells which, when ligated, lead to the repression of cytolytic T-cell expansion or activity (2). Antibodies preventing the ligation of both receptors have shown marked antitumor activity and have received Food and Drug Administration approval for the treatment of several malignancies (1).

One such antibody specific for PD-1 is pembrolizumab (Keytruda; Merck), a humanized IgG4 monoclonal antibody approved for the treatment of advanced melanoma and non–small cell lung cancer, and with early promising results observed in other malignancies as well (3). In clinical trials, pembrolizumab displayed a 32% overall response rate in melanoma patients previously treated with ipilimumab, 21% higher than the response rate of patients receiving traditional chemotherapy (4,5). However, despite fewer toxicities than ipilimumab and traditional chemotherapies, excessive accumulation of PD-1 antibodies in the liver and kidneys has limited the use of these agents in some patients (6). Because only a subset of patients responds to anti–PD-1 therapies, and because their use is not without the risk of side effects, more work is needed to better understand the pharmacokinetic properties of these antibodies in vivo to identify optimal dosing strategies to provide the best chance of clinical benefit. Additionally, the ability to monitor PD-1 levels and localization in a dynamic fashion using a noninvasive imaging modality could prove useful at predicting for and monitoring responses to PD-1–targeted therapies.

There have been limited investigations into the imaging of checkpoint blockades. Recently, two studies used different murine PD-1 antibodies, radiolabeled with ^{64}Cu, for imaging PD-1–expressing tumor-infiltrating lymphocytes in murine models of melanoma (7,8). In this work, we investigate the biodistribution of a humanized PD-1 antibody in vivo. To our knowledge, this is the first study to investigate the pharmacokinetics, biodistribution, and

dosimetry of radiolabeled pembrolizumab, a humanized antibody targeting PD-1, in vivo. To that end, we used PET imaging to map the biodistribution of pembrolizumab radiolabeled with the positron-emitting radionuclide ^{89}Zr in two normal rodent models. These data were extrapolated to human subjects to estimate radiation dosimetry to normal tissues. Additionally, the biodistribution and pharmacokinetics were assessed in a humanized mouse model implanted with human peripheral blood mononuclear cells (PBMCs). The humanized model showed a biodistribution profile differing from normal mice, allowing for effective visualization and mapping of PD-1–expressing cells in vivo using noninvasive PET imaging.

MATERIALS AND METHODS

In Vitro Binding Assay

Human PBMCs were isolated from blood samples collected under an institutional review board–approved protocol from patients giving informed consent via density gradient centrifugation using Ficoll-Histopaque (GE Healthcare). PBMCs were thawed, washed, and resuspended at a concentration of 2×10^6 cells/mL in AB Media (RPMI-1640 + 10% AB sera/2% penicillin–streptomycin/1% NaPyr/0.1% βME) and stimulated with phorbol myristate acetate (40 ng/mL; Sigma) and ionomycin (1.3 ug/mL; MP Biomedicals) for 18 h. Cells were washed and stained with the indicated concentration of pembrolizumab or deferoxamine (Df)-pembrolizumab for 1 h at 4°C. Cells were then washed and stained with AlexaFluor488-antihuman IgG secondary antibody (2 μg/mL; Life Technologies) as well as CD3-v500, CD4-PE, and CD8-APC antibodies (BD Biosciences) at a concentration of 2 tests/mL and a 1:1,000 dilution of GhostDye Red-780 (Tonbo Biosciences). Cells were washed, resuspended in FACS Wash (phosphate-buffered saline/3% fetal calf serum), and analyzed on a LSRFortessa cytometer (BD Biosciences). The gating strategy was Alive/FSCxSSC/singlets/CD3+ and CD4 or CD8+. The PD-1–positive gate was determined using both no primary and no secondary antibody control-stained samples.

Conjugation and ^{89}Zr Labeling of Pembrolizumab

Pembrolizumab was obtained commercially (Merck & Co., Inc.) and conjugated with p-SCN-deferoxamine (Macrocyclics) using a method previously reported (9,10). ^{89}Zr was produced in a biomedical cyclotron (PETtrace; GE Healthcare) via irradiation of natural yttrium foils (250 μm, 99.9%) with 16.4-MeV protons as previously described (11). Radiolabeling of Df-pembrolizumab with ^{89}Zr was accomplished using traditional methods previously described and purified with PD-10 columns (GE Healthcare) (12).

Animal Models

All animal studies were conducted under a protocol approved by the University of Wisconsin Institutional Animal Care and Use Committee. Mice and rats were used for examining the biodistribution, pharmacokinetics, and dosimetry of ^{89}Zr-Df-pembrolizumab in vivo. Five-week-old female ICR (CD-1) mice and 5-wk-old Hsd: Sprague–Dawley outbred rats were obtained from Harlan Laboratories. Six-week- to 8-wk-old nonobese diabetic severe combined immuno-deficient (SCID) γ-(NSG) mice and NSG mice engrafted with human peripheral blood lymphocytes (hu-PBL-SCID) were obtained from the University of Wisconsin–Madison Humanized Mouse Core Service.

PET Imaging of ^{89}Zr-Df-Pembrolizumab

PET scans were acquired on an Inveon microPET/micro-CT rodent model scanner (Siemens Medical Solutions). Mice were intravenously injected with 5−10 MBq of ^{89}Zr-Df-pembrolizumab for imaging. Rats received a 37-MBq intravenous dose of ^{89}Zr-Df-pembrlizumab. For whole-body rat imaging, 30-min PET scans were acquired using a continuous bed motion method. A total of 30 passes through a 30-cm

transaxial field of view were recorded. Rat reconstructions were performed using the 2-dimensional ordered-subset expectation maximization reconstruction. For mice, 40 million coincidence events static scans were recorded, and images were reconstructed using the 3-dimensional ordered-subset expectation maximization algorithm. Region-of-interest (ROI) analysis of the images was performed to determine tracer uptake in major organs or tissues using the Inveon Research Workplace software (Siemens Medical Solutions). Quantitative results are given as percentage injected dose per gram of tissue (%ID/g).

Biodistribution of ^{89}Zr-Df-Pembrolizumab in Mice and Rats

Biodistribution was performed after the final PET scans. Major organs, tissues, and blood were collected, and the radioactivity in each sample was measured using a WIZARD2 automatic γ-counter (PerkinElmer) and recorded as %ID/g (mean ± SD).

Immunohistochemistry

Salivary glands were extracted from mice and embedded in Tissue-Tek optimal-cutting-temperature compound (Sakura Finetek). Frozen tissue slices of 5-μm thickness were fixed with 4% paraformaldehyde for 10 min and rehydrated in phosphate-buffered saline (PBS). Slides were blocked (10% normal donkey serum in 0.2% Triton-X in PBS) for 30 min at 23°C. Dilutions (1:200) of rabbit antihuman CD3 (Novus Biologicals) and goat antihuman PD1 (R&D Systems) were prepared in the blocking solution and incubated with the tissue for 12 h at 4°C. Slides were washed 3 times with PBS for 15 min. Secondary antibodies were prepared at dilutions of 1:1,000 for donkey-anti rabbit IgG DyLight 550 and 1:4,000 for donkey anti-goat IgG DyLight 488 (Novus Biologicals) and incubated with the tissue for 1 h. Slides were washed 2 times with 0.2% Triton-X in PBS and 2 times with PBS for 15 min. Slides were mounted with Vectashield antifade mounting medium with 4′,6-diamidino-2-phenylindole (DAPI) and coverslipped before being imaged with the Nikon A1RS system.

Radiation Dosimetry Extrapolation to Humans

Dosimetry analysis was performed using OLINDA/EXM software (13). Estimated human dosimetry was calculated on the basis of average %ID/g values from the serial PET scans on both mice and rats, which were converted to %ID in humans. It was assumed that the biodistribution in adult humans was the same as in the animal models, and a monoexponential model was used for the time–activity curves. OLINDA provides effective dose outputs; thus, weighting factors from International Commission on Radiological Protection Publication 103 were used to convert to absorbed dose in each organ (14).

Statistical Analysis

Quantitative data were expressed as mean ± SD with all error bars denoting the SD. Means were compared using the Student t test, and P values of less than 0.05 were considered statistically significant.
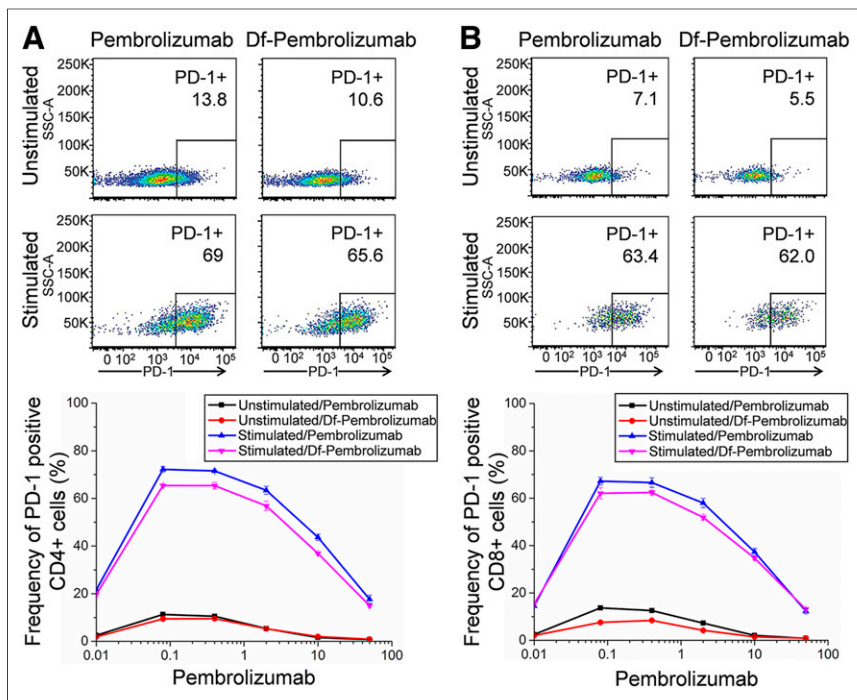
RESULTS

Binding of Pembrolizumab to CD4+ and CD8+ T-Cells

A binding assay of pembrolizumab to CD4+ and CD8+ T-cells was performed to ensure that that Df chelation of pembrolizumab did not hinder or alter its binding affinity or specificity. T-cells were stimulated for 18 h before the addition of pembrolizumab or Df-pembrolizumab. Chelated pembrolizumab was shown to bind specifically to activated CD4+ T-cells, and that chelation did not substantially alter its binding affinity for these activated cells (Fig. 1A). Similar results were observed for CD8+ T-cells (Fig. 1B).

### Chelation and Radiolabeling of Pembrolizumab

After radiolabeling, the purified ^{89}Zr-Df-pembrolizumab was shown to be labeled with a specific activity of 740 MBq/mg antibody.

FIGURE 1. Cell binding assay of pembrolizumab to CD4+ and CD8+ T-cells. CD4+ and CD8+ T-cells were stimulated to express PD-1. In CD4+ T-cells (A) and CD8+ T-cells (B), both pembrolizumab and Df-pembrolizumab displayed similar binding efficiency, suggesting that chelation of the antibody did not affect binding of antibody to PD-1. Also, pembrolizumab displayed significantly higher binding to stimulated T-cells expressing the PD-1 receptor, demonstrating specificity of antibody.

Labeling efficiency was determined by instant thin-layer chromatography and shown to be greater than 60%. Mice were injected with a lower activity of ^{89}Zr-Df-pembrolizumab (5–10 MBq) in comparison to rats (37 MBq).
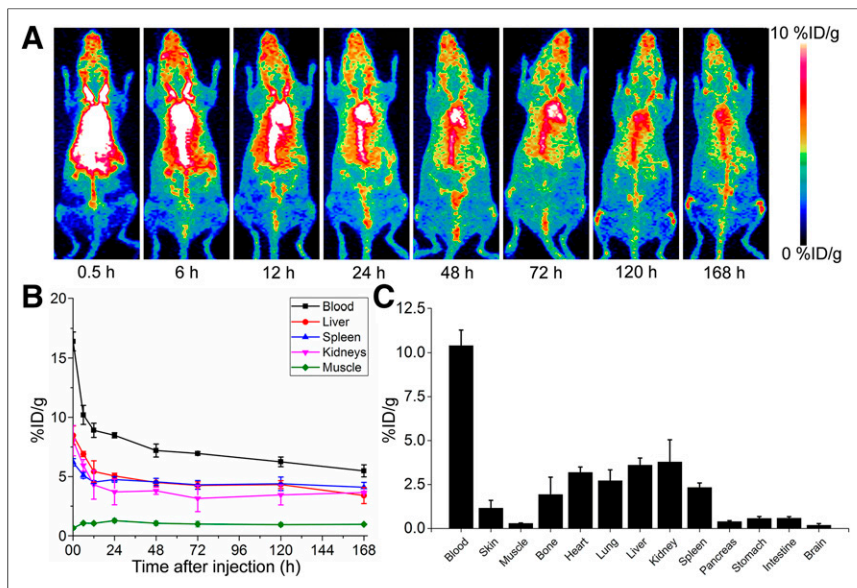
FIGURE 2. Whole-body PET imaging, quantitative PET analysis, and biodistribution of ^{89}Zr-Df-pembrolizumab in ICR mice. (A) Maximum-intensity projections are shown after injection, with scale ranging from 0 to 10 %ID/g. (B) PET ROI analysis is shown as time–activity curves of blood, liver, spleen, kidneys, and muscle after intravenous injection of ^{89}Zr-Df-pemrolizumab (n = 4). (C) Biodistribution of ^{89}Zr-Df-emrolizumab in blood, organs, and tissues of mice at 168 h after injection (n = 4).
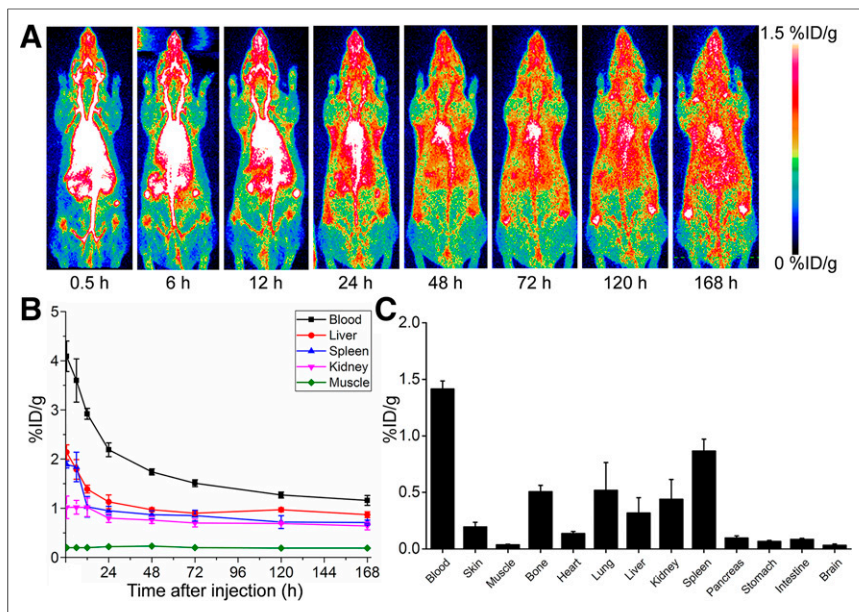
PET Imaging and Biodistribution of ^{89}Zr-Df-Pembrolizumab in Mice

Longitudinal PET imaging studies were performed for 7 d followed by animal euthanasia for biodistribution studies. Sequential PET images are presented as maximum-intensity projections (Fig. 2A). ROI analysis of PET imaging was used to quantify the biodistribution (Fig. 2B; Supplemental Table 1 [supplemental materials are available at http://jnm.snmjournals.org]). At the first time point, the blood pool showed an elevated accumulation of ^{89}Zr-Df-pembrolizumab (16.4 ± 0.8 %ID/g at 0.5 h after injection; n = 4), which decreased gradually with a clearance half-life of 38 h. Initial accumulation in the liver and spleen were shown to be 8.48 ± 0.79 and 6.20 ± 0.31 %ID/g, respectively (n = 4). Although the liver displayed a 50% decrease in %ID/g from 6 to 168 h, the spleen showed less removal with only approximately 20% of the tracer being cleared by 168 h after injection. Minimal uptake of the tracer was found in muscle and brain tissues. After the terminal PET scans at 168 h after injection, mice were euthanized for biodistribution studies to validate the PET imaging data. Ex vivo biodistribution confirmed that ^{89}Zr-Df-pembrolizumab remained stable in blood circulation at 168 h after injection (Fig. 2C). The quantitative PET analysis of the liver, spleen, and kidneys showed similar %ID/g at 168 h after injection. Organs with the lowest accumulation of ^{89}Zr-Df-pembrolizumab at 168 h were the pancreas, stomach, intestines, and brain.

PET Imaging and Biodistribution of ^{89}Zr-Df-Pembrolizumab in Rats

Longitudinal PET imaging studies were performed for 7 d, and representative maximum-intensity projections were obtained for analysis (Fig. 3A). The blood circulation of ^{89}Zr-Df-pembrolizumab was highest at 0.5 h (4.09 ± 0.31 %ID/g) and gradually decreased by 4-fold to 1.16 ± 0.10 %ID/g by 168 h after injection (Fig. 3B; Supplemental Table 2; n = 4). The liver and spleen showed similar accumulation of 2.14 ± 0.15 and 1.89 ± 0.07 %ID/g at 0.5 h, respectively. Unlike mice, the liver did not show the enhanced removal of ^{89}Zr-Df-pembrolizumab in comparison to the spleen. The liver and spleen showed similar tracer uptake values of 0.87 ± 0.06 and 0.71 ± 0.05 %ID/g at 168 h, respectively (n = 4). Also, the %ID/g of ^{89}Zr-Df-pembrolizumab was determined in the lungs, intestines, ovaries, and brain through PET analysis. Lung accumulation remained relatively constant throughout the entire study. Interestingly, tracer uptake was high in the ovaries, suggesting high nonspecific binding in ovarian
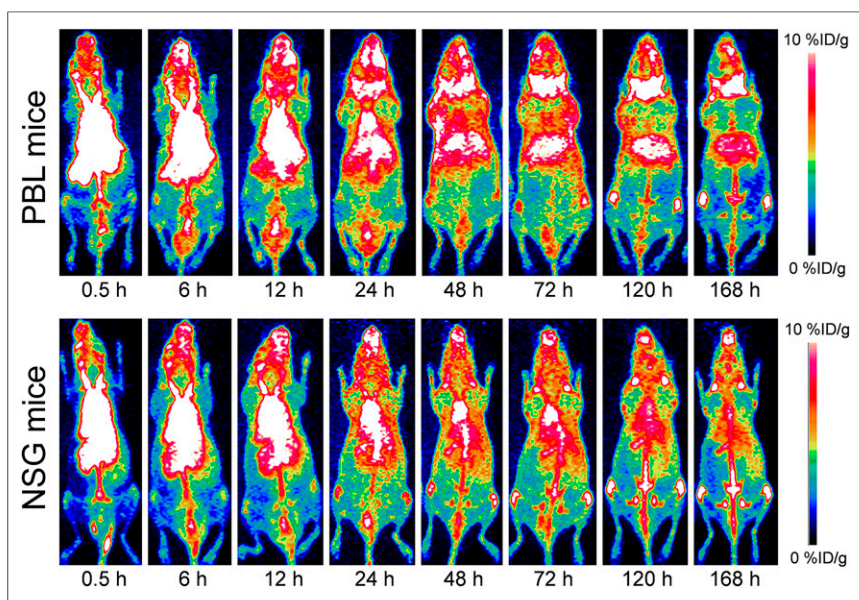
FIGURE 3. Whole-body PET imaging, quantitative PET analysis, and biodistribution of ^{89}Zr-Df-pembrolizumab in Sprague–Dawley rats. (A) Maximum intensity projections are shown after injection, with scale ranging from 0 to 1.5 %ID/g. (B) PET ROI analysis is shown as time–activity curves of blood, liver, spleen, kidneys, and muscle after intravenous injection of ^{89}Zr-Df-pembrolizumab ($n = 4$). (C) Biodistribution of ^{89}Zr-Df-pembrolizumab in blood, organs, and tissues of rats at 168 h after injection ($n = 4$).

tissues. The initial accumulation of ^{89}Zr-Df-pembrolizumab was 1.13 ± 0.05 %ID/g and slightly decreased to 0.86 ± 0.19 %ID/g by 168 h after injection ($n = 4$). Ex vivo biodistribution showed findings similar to the PET imaging data, with the blood pool displaying the highest radioactivity at 168 h after injection (Fig. 3C). In addition, the liver, spleen, and kidneys showed similar accumulation, with muscle having the lowest uptake. In both mice and rats, bone uptake was similar

to uptake in the liver, spleen, and kidneys. This phenomenon was expected, because nonchelated ^{89}Zr displays a strong affinity for phosphate and acts as a bone seeker in vivo (*15*).

PET Imaging of PD-1 Expression in Humanized Murine Model

As a proof of concept, the biodistribution of ^{89}Zr-Df-pembrolizumab was mapped in NSG and hu-PBL-SCID mice. PBL mice were generated by engrafting 10^6 human PBMCs into 4- to 6-wk-old NSG mice. Thus, the PBL model was used to demonstrate that ^{89}Zr-Df-pembrolizumab may function as a potential radiotracer for imaging of PD-1 expression in vivo. PET imaging of NSG and PBL mice showed similar findings in most organs, including the spleen, kidney, and muscle tissues (Fig. 4; Supplemental Tables 3 and 4). However, there were two main differences between the tracer biodistribution in PBL and NSG mice (Figs. 5A and 5B). First, PBL mice showed a shorter blood circulation in comparison to NSG mice. A statistically significant difference was found between the blood-pool activity of NSG (9.78 ± 0.80 %ID/g) and PBL (6.13 ± 0.41 %ID/g) mice at 48 h and continued through 168 h after injection ($n = 4$). Second, the PBL mice displayed high uptake in the salivary glands. This difference in tracer accumulation was statistically significant at 6 h and each time point afterward (Fig. 5C). Last, ex vivo distribution confirmed the PET imaging data, showing differences in tracer uptake by the blood pool and salivary glands (Supplemental Fig. 1). In addition, biodistribution showed a significant difference in liver accumulation, which could not be effectively delineated through PET ROI analysis (Fig. 5D). Histologic studies further validated that the salivary glands of PBL mice contained human T-cells expressing PD-1 through staining of the T-cell marker CD3 and PD-1, whereas NSG mice showed minimal staining as expected (Fig. 6).
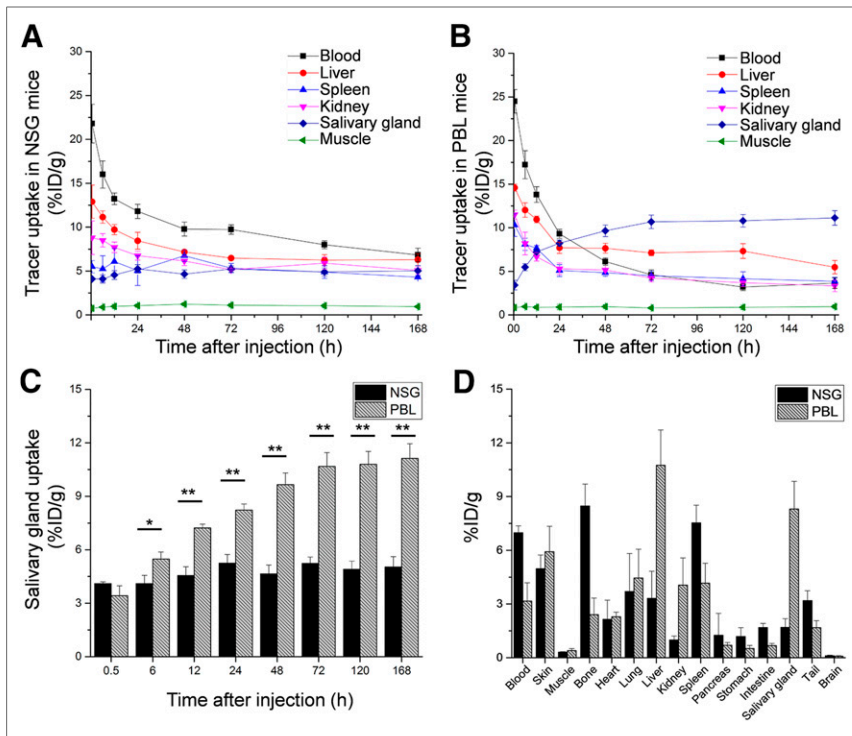
Radiation Dosimetry

Estimations of human absorbed doses to normal tissues, based on the biodistribution of ^{89}Zr-Df-pembrolizumab in mice and rats, are summarized in Supplemental Tables 5 and 6. The calculated dosimetry data were markedly similar between mice and rats, which showed relatively higher doses to the liver (0.811 mGy/MBq in mice and 0.958 mGy/MBq in rats) and urinary bladder wall (0.512 mGy/MBq in mice and 0.578 mGy/MBq in rats). Low doses to the kidneys (0.025 mGy/MBq in mice and 0.017 mGy/MBq in rats) were calculated. Interestingly, the dose to

FIGURE 4. PET imaging of PBL mice (NSG mice reconstituted with human PBMCs) and normal NSG mice after injection of 37 MBq of ^{89}Zr-Df-pembrolizumab. Maximum-intensity projections of representative mice are shown at several time points after injection.

FIGURE 5. Quantitative analysis of PET data and biodistribution of ^{89}Zr-Df-pembrolizumab in PBL mouse model reconstituted with human PBMCs and normal NSG mice. (A) PET ROI analysis is shown as time–activity curves of blood, liver, spleen, kidneys, and muscle after intravenous injection of ^{89}Zr-Df-pembrolizumab in NSG mouse model ($n = 4$). (B) PET ROI analysis is shown as time–activity curves of blood, liver, spleen, kidneys, and muscle after intravenous injection of ^{89}Zr-Df-pembrolizumab in PBL mice ($n = 4$). (C) Comparison of salivary gland uptake of ^{89}Zr-Df-pembrolizumab between NSG and PBL mice ($n = 4$). (D) Biodistribution of ^{89}Zr-Df-pembrolizumab in blood, organs, and tissues of NSG and PBL mice at 168 h after injection ($n = 4$). *$P < 0.05$. **$P < 0.01$.

the ovaries was highest, which may be of concern given the high radiosensitivity of the gonads. The total whole-body effective dose (0.515 ± 0.005 from mice and 0.540 ± 0.008 from rats) from the administered ^{89}Zr-Df-pembrolizumab is far less than that received from typical abdominal CT scans. Similarly, NSG and PBL dosimetry showed high doses to the liver (1.207 mGy/MBq in PBL and 1.196 mGy/MBq in NSG mice) and ovaries (1.591 mGy/MBq in

FIGURE 6. Histologic staining of salivary tissue sections from PBL and NSG mice to confirm presence of PD-1 and T-cells (CD3$^+$). Scale bar, 20 µm.

PBL and 1.594 mGy/MBq in NSG mice), as shown in Table 1. A key difference in tracer biodistribution was the elevated uptake observed in the salivary glands of PBL mice, which resulted in higher total-body doses to PBL mice (1.246 mGy/MBq vs. 0.838 mGy/MBq for PBL and NSG mice, respectively).

DISCUSSION

Detailed investigation of the pharmacokinetic properties of therapeutic antibodies remains critical to their successful clinical translation. Although antibodies blocking T-cell checkpoint pathways have been shown to elicit strong antitumor immune responses, only a subset of patients develop an objective response to these therapies. The original clinical investigation of pembrolizumab for the treatment of melanoma showed that only 21 of 89 (24%) patients developed an objective antitumor response, with similar response rates reported in the many subsequent clinical trials (16). For this reason, researchers are investigating several avenues for improving the tumor accumulation of antibodies with the hope of increasing patient response rates. Central to these experiments is a means by which to assess the trafficking and biodistribution of these antibodies in preclinical models. We report here the first known use of a ^{89}Zr-labeled PD-1 antibody as a radiotracer in rodent models. We used PET imaging to monitor antibody organ uptake over time and used these results to estimate human dosimetry from these data. Further, we demonstrated in a humanized mouse model the specific binding of ^{89}Zr-Df-pembrolizumab to activated T-cells infiltrating the salivary gland.

One important limitation of this work is that several studies have shown that preclinical investigation of antibody biodistribution in rodent models greatly varies from the observed kinetics in human patients (17). High uptake in the liver and spleen in both mice (Fig. 2) and rats (Fig. 3) were likely a result of expected nonspecific binding and hepatobiliary clearance (18). These intramodel differences are a limitation to the successful translation of some therapeutic antibodies, yet data obtained from rodent models may be extrapolated to humans through dosimetry analysis. This provides essential information regarding the expected human internal radiation doses to normal organs associated with the administration of radiolabeled antibodies. Although all animals maintain similar biologic machinery for the metabolism and elimination of drugs, these metabolic capabilities differ between different animal species (17). For example, it has been
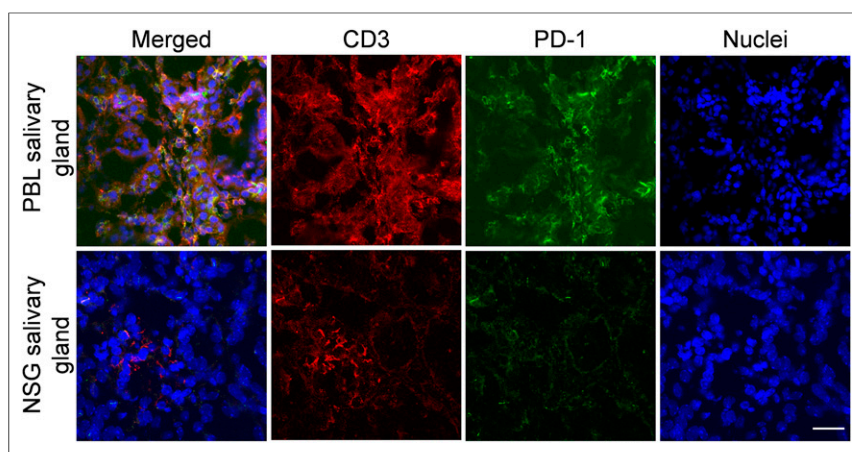
TABLE 1
Estimated Radiation-Absorbed Doses to Adult Human After Intravenous Injection of ^{89}Zr-Df-Pembrolizumab in PBL and NSG Mice (n = 4)

Organ	PBL model (NSG mice with human PBMCs)				NSG mice			
	mGy/MBq	SD	rad/mCi	SD	mGy/MBq	SD	rad/mCi	SD
Adrenals	0.028	0.001	0.104	0.001	0.028	0.001	0.105	0.001
Brain	0.249	0.005	0.919	0.019	0.245	0.006	0.905	0.022
Breasts	0.185	0.001	0.683	0.005	0.185	0.002	0.684	0.008
Small intestine	0.025	0.001	0.091	0.001	0.025	0.001	0.091	0.001
Stomach wall	0.630	0.004	2.329	0.014	0.630	0.005	2.332	0.019
Kidneys	0.030	0.001	0.113	0.005	0.035	0.001	0.128	0.005
Liver	1.207	0.022	4.465	0.083	1.196	0.061	4.426	0.225
Lungs	0.556	0.004	2.059	0.016	0.562	0.003	2.078	0.010
Muscle	0.019	0.001	0.070	0.002	0.019	0.001	0.072	0.001
Ovaries	1.591	0.006	5.885	0.023	1.594	0.013	5.897	0.046
Pancreas	0.029	0.001	0.108	0.001	0.029	0.001	0.108	0.002
Red marrow	0.533	0.003	1.970	0.010	0.533	0.004	1.972	0.014
Skin	0.373	0.002	1.380	0.008	0.373	0.003	1.378	0.012
Spleen	0.030	0.001	0.112	0.002	0.028	0.007	0.104	0.027
Thymus	0.024	0.001	0.087	0.101	0.024	0.013	0.089	0.048
Salivary glands	1.246	0.082	4.609	0.013	0.838	0.004	3.099	0.014
Urinary bladder wall	0.573	0.004	2.118	0.001	0.574	0.001	2.125	0.002
Uterus	0.026	0.001	0.097	0.001	0.026	0.001	0.097	0.001
Total-body effective dose (mSv/MBq)	0.597	0.005			0.581	0.003		

shown that mice and rats display enhanced biliary excretion rates, whereas humans and other primates exhibit poor biliary excretion of most drugs (17,19). Dosimetry data may help predict potential toxicities before they occur in humans, while also assisting scientists in determining optimal initial dosing strategies when needed. The pattern of absorbed dose values obtained in this study indicates that this agent localizes in several tissues, further confirming the optimal circulation and low toxicity profile found in clinical trials.

As a proof of concept, we demonstrated that ^{89}Zr-Df-pembrolizumab could be used for the noninvasive imaging of PD-1 expression. Currently, there are limited animal models for immunoimaging studies. PBL mice are a humanized murine model created by engrafting human PBMCs in NSG mice (20). Although these humanized mice gradually develop allogenic graft versus host disease, limiting their use for many therapy studies, the upregulation of PD-1 during acute graft versus host disease made it possible to image the biodistribution of this immunotherapy target in our case (21). Similar to our findings, several research groups have reported that engrafted immune cells infiltrate the salivary glands and lacrimal glands in PBL mice (22–24). Thus, we expected that the PD-1–expressing T-cells would localize in the salivary glands of PBL mice, verifying that our PD-1 tracer was effective for imaging of PD-1–expressing T-cells in vivo. In this study, the salivary glands of PBL mice displayed the highest uptake of ^{89}Zr-Df-pembrolizumab of 11.13 ± 0.82 %ID/g at 168 h after injection, whereas NSG mice showed only 5.03 ± 0.59 %ID/g at the same time point (Fig. 5; n = 4). Thus, this study successfully demonstrated the ability to use a noninvasive immunotherapeutic-based imaging

agent to monitor PD-1 localization and expression in vivo. This could allow researchers to potentially evaluate T-cell trafficking in vivo, and possibly to monitor for evidence of autoimmune adverse events by accumulation of PD-1–specific tracer at target sites before the development of overt symptoms. Further, we demonstrated that the use of humanized animal models may provide unique avenues for further imaging investigations of cancer immunotherapies.

In the future, an investigation into the correlation between PD-1 expression and tracer uptake may provide insight into methods for enhancing treatment protocols, further enhancing potential patient stratification. The future of immunotherapy is continually expanding, as researchers search for novel immune checkpoint molecules beyond PD-1 and CTLA-4. Some heavily investigated candidates include T-cell immunoglobulin mucin-3, B and T lymphocyte attenuator, and lymphocyte activation gene-3 (25). Central to the clinical development of these novel T-cell checkpoint antibodies are questions surrounding proper dosage and timing, in addition to identifying patient populations more likely to respond to these therapies. We believe the use of radiolabeled variants of these antibodies for noninvasive PET imaging, specifically in the humanized PBL mouse model, could provide useful predictive data to assist in the clinical development of these novel immunotherapy agents.

CONCLUSION

Herein, this study provided the initial evidence that radiolabeled pembrolizumab circulates in animal models for an extended

period, accumulating in expected tissues and organ systems. The pharmacokinetics, biodistribution, and dosimetry were explored in two rodent models and showed that ^{89}Zr-Df-pembrolizumab is appropriate for tracking the fate of pembrolizumab in vivo. In addition, this study verified that PD-1 expression can be noninvasively imaged using ^{89}Zr-Df-pembrolizumab in a humanized murine model. These data may assist researchers in assessing the treatment efficacy of immunotherapy in vivo, while also simplifying the process of patient stratification for potential future clinical applications.

DISCLOSURE

REFERENCES

1. Topalian SL, Taube JM, Anders RA, Pardoll DM. Mechanism-driven biomarkers to guide immune checkpoint blockade in cancer therapy. *Nat Rev Cancer.* 2016;16:275–287.
2. Kyi C, Postow MA. Checkpoint blocking antibodies in cancer immunotherapy. *FEBS Lett.* 2014;588:368–376.
3. Dolan DE, Gupta S. PD-1 pathway inhibitors: changing the landscape of cancer immunotherapy. *Cancer Control.* 2014;21:231–237.
4. Johnson DB, Peng C, Sosman JA. Nivolumab in melanoma: latest evidence and clinical potential. *Ther Adv Med Oncol.* 2015;7:97–106.
5. Robert C, Schachter J, Long GV, et al. Pembrolizumab versus ipilimumab in advanced melanoma. *N Engl J Med.* 2015;372:2521–2532.
6. Khoja L, Butler MO, Kang SP, Ebbinghaus S, Joshua AM. Pembrolizumab. *J Immunother Cancer.* 2015;3:36–45.
7. Natarajan A, Mayer AT, Xu L, Reeves RE, Gano J, Gambhir SS. Novel radiotracer for immunoPET imaging of PD-1 checkpoint expression on tumor infiltrating lymphocytes. *Bioconjug Chem.* 2015;26:2062–2069.
8. Hettich M, Braun F, Bartholomä MD, Schirmbeck R, Niedermann G. High-resolution PET imaging with therapeutic antibody-based PD-1/PD-L1 checkpoint tracers. *Theranostics.* 2016;6:1629–1640.
9. Vosjan MJ, Perk LR, Visser GW, et al. Conjugation and radiolabeling of monoclonal antibodies with zirconium-89 for PET imaging using the bifunctional chelate p-isothiocyanatobenzyl-desferrioxamine. *Nat Protoc.* 2010;5:739–743.
10. Perk LR, Vosjan MJ, Visser GW, et al. p-Isothiocyanatobenzyl-desferrioxamine: a new bifunctional chelate for facile radiolabeling of monoclonal antibodies with zirconium-89 for immuno-PET imaging. *Eur J Nucl Med Mol Imaging.* 2010; 37:250–259.
11. Holland JP, Sheh Y, Lewis JS. Standardized methods for the production of high specific-activity zirconium-89. *Nucl Med Biol.* 2009;36:729–739.
12. Hernandez R, Sun H, England CG, et al. ImmunoPET imaging of CD146 expression in malignant brain tumors. *Mol Pharm.* 2016;13:2563–2570.
13. Stabin MG, Sparks RB, Crowe E. OLINDA/EXM: the second-generation personal computer software for internal dose assessment in nuclear medicine. *J Nucl Med.* 2005;46:1023–1027.
14. International Commission on Radiological Protection (ICRP). The 2007 recommendations of the international commission on radiological protection. ICRP publication 103. *Ann ICRP.* 2007;37:1–332.
15. Abou DS, Ku T, Smith-Jones PM. In vivo biodistribution and accumulation of ^{89}Zr in mice. *Nucl Med Biol.* 2011;38:675–681.
16. Rajakulendran T, Adam DN. Spotlight on pembrolizumab in the treatment of advanced melanoma. *Drug Des Devel Ther.* 2015;9:2883–2886.
17. Sharma V, McNeill JH. To scale or not to scale: the principles of dose extrapolation. *Br J Pharmacol.* 2009;157:907–921.
18. Casey JL, King DJ, Pedley RB, et al. Clearance of yttrium-90-labelled antitumour antibodies with antibodies raised against the 12N4 DOTA macrocycle. *Br J Cancer.* 1998;78:1307–1312.
19. Lin JH. Applications and limitations of interspecies scaling and in vitro extrapolation in pharmacokinetics. *Drug Metab Dispos.* 1998;26:1202–1212.
20. Brehm MA, Shultz LD, Greiner DL. Humanized mouse models to study human diseases. *Curr Opin Endocrinol Diabetes Obes.* 2010;17:120–125.
21. Gallez-Hawkins GM, Thao L, Palmer J, et al. Increased programmed death-1 molecule expression in cytomegalovirus disease and acute graft-versus-host disease after allogeneic hematopoietic cell transplantation. *Biol Blood Marrow Transplant.* 2009;15:872–880.
22. Young NA, Wu LC, Bruss M, et al. A chimeric human-mouse model of Sjogren's syndrome. *Clin Immunol.* 2015;156:1–8.
23. Nervi B, Rettig MP, Ritchey JK, et al. Factors affecting human T cell engraftment, trafficking, and associated xenogeneic graft-vs-host disease in NOD/SCID beta2mnull mice. *Exp Hematol.* 2007;35:1823–1838.
24. Levy S, Nagler A, Okon S, Marmary Y. Parotid salivary gland dysfunction in chronic graft-versus-host disease (cGVHD): a longitudinal study in a mouse model. *Bone Marrow Transplant.* 2000;25:1073–1078.
25. Le Mercier I, Lines JL, Noelle RJ. Beyond CTLA-4 and PD-1, the generation Z of negative checkpoint regulators. *Front Immunol.* 2015;6:1–15.